www.sciencemag.org/content/358/6361/369/suppl/DC1

Supplementary Materials for

Learning-enhanced coupling between ripple oscillations in association cortices and hippocampus

Dion Khodagholy,* Jennifer N. Gelinas,* György Buzsáki†

*These authors contributed equally to this work.
†Corresponding author. Email: gyorgy.buzsaki@nyumc.org

Published 20 October 2017, *Science* **358**, 369 (2017)
DOI: 10.1126/science.aan6203

This PDF file includes:

Materials and Methods
Figs. S1 to S9
References

Supplementary Materials:

Materials and Methods

Probe fabrication and preparation: The fabrication of conducting polymer-based NeuroGrids has been discussed in previous publications *(15,16)*. In brief, a projection exposure system was used to pattern parylene C, Au, Pt, Ti and PEDOT:PSS films.

A thin Ti layer (60 nm) was sandwiched between two 1 μm-thick parylene C (SCS Labcoater 2) films to act as an ion barrier over large surfaces. To avoid residues of organic particles on the etched surfaces as a result of extracting large volume of materials, the etching areas were protected and pre-patterned using a 250 nm photoresist (S1805). This ensured reliable mechanical and electrical interface for pads and electrodes, respectively. A lift-off process was used to pattern metal pads and interconnects. AZ nLOF 2020 (a negative photoresist) was spin-coated on the parylene film (5,500 r.p.m.), baked at 115 °C for 60 sec, exposed using a stepper (GCA Autostep 200 DSW i-line Wafer Stepper), and finally developed (MF726 developer). With use of an e-beam metal evaporator (CVC SC4500 at 2.10^{-6} bars), metallic layers of Ti (10 nm), Pt (150 nm) and Au (50nm) were deposited. Lift-off was performed using 1165 stripper (2 hours).

We employed 3-(trimethoxysilyl)propyl methacrylate as an adhesion promoter and a dilute solution of industrial cleaner (Micro-90) as an anti-adhesion agent for parylene films. The film was patterned with a 4.5 μm thick layer of SPR220-45 (Electronic Materials) photoresist and dry etched with a plasma reactive-ion etching process (Oxford 80 plus; 180 W, 50 sccm O2, 3 sccm SF6, 2 sccm CF4 for 15 min).

To enhance the conductivity of PEDOT:PSS, a mixture of PEDOT:PSS aqueous dispersion (PH-1000 from H.C. Stark) and ethylene glycol (20:5 ml ratio) was prepared and mixed with dodecyl benzene sulfonic acid (100 μl per 50 ml) and 3 glycidoxypropyltrimethoxysilane (1 wt%) to adjust surface energy and cross link, respectively. The resulting dispersion was spin-coated in two steps with soft-bake in between (120C, 60 s) at 650 rpm.

The films were subsequently baked at 140 °C for 1 h and then immersed in deionized water overnight to remove any excess low-molecular weight compounds. The electrodes were characterized *in vitro* using phosphate buffer solution (PBS) solution. A significantly larger Ag/AgCl wire compared to electrode geometry served as the reference electrode for impedance spectroscopy and measurements.

The NeuroGrid was attached to a custom printed circuit board via a zero insertion force (ZIF) connector. The board contained two or four (120 or 240 channels) RHD2164 dies (Intan Technologies), directly wire-bonded to the board for the purpose of amplification, digitization and transmission of the acquired neural signals via a serial peripheral interface (SPI) protocol to a computer interface board (RHD2000 evaluation board; Intan Technologies). All back-end electronics were covered with silicone elastomer as an encapsulation layer.

Animal surgical procedures: All animal experiments were approved by the Institutional Animal Care and Use Committee at New York University Langone Medical Center (NYULMC).

Sixteen male Long–Evans rats (200–350 g, 8–15 weeks of age) were used for intracranial implantation. No rats were excluded from analysis. Rats were kept on a regular 12 h–12 h light–dark cycle and housed in pairs before implantation, but separated afterward. No prior experimentation had been performed on these rats.

The animals were initially anaesthetized with 2% isoflurane and maintained under anesthesia with 0.75–1% isoflurane during the surgery.

For large-scale NeuroGrid implantations (n = 3), a large cranial window bordered by the hemispheric sutures (~ 5 x 9 mm^2) was opened followed by dura-mater incision and placement of the NeuroGrid on the pial surface of the brain. To minimize brain swelling and inflammation, methylprednisolone (30mg/kg) was administered intramuscularly during surgery.

For high-density NeuroGrid implantations (n = 10), a 3x3 mm^2 cranial window over parietal cortex (AP -4.0 ML 3.5) was opened followed by dura-mater removal and placement of the NeuroGrid on the pial surface of the brain. An implantable silicon probe was then inserted into the hippocampus through perforations in the NeuroGrid (AP -3.5, ML 3.0) and depth adjusted based on detection of hippocampal ripples. In an additional 3 animals, silicon probes or wire arrays were inserted into mPFC (AP +3.5, ML 0.2-1.0, DV -3.0) in combination with a high-density NeuroGrid and/or hippocampal silicon probe.

After all surgical procedures, the craniotomies were covered with gel-foam and sealed using a silicone elastomer.

Once the rats had recovered for 5 days post-surgical procedure, a subset underwent sensory evoked potential testing. Visual evoked potentials were performed by pulsing an LED light source at 3 s intervals with 1 ms duration in a reflective sleep-box to ensure omnidirectional light exposure. Data were synchronized through an auxiliary digital channel marking the exposure time. Somatosensory evoked potentials were performed by insertion of two 36 AWG gold plated wires into the hind limb of the rat contralateral to the cranial window under isoflurane anesthesia. Current pulses with 1ms duration were titrated until movement of the digits was visually observable. Pulses were repeated every 3 s for 10-15 minutes.

Behavioral protocol:

Animals. Ten rats were used for behavioral experiments in addition to neurophysiological recordings. These animals were placed on a water-deprivation schedule for 3–5 d before undergoing intracranial implantation for familiarization with obtaining water via a handheld syringe administered by the experimenter. Rats were weighed daily during the water-deprivation stage to ensure that body weight did not decrease to <85% of pre-deprivation measurements. After the postoperative recovery period, rats were placed back on the water-deprivation schedule for further behavioral training. Rats first underwent neurophysiological recordings in the home-cage during periods of intermixed sleep and free behavior. Six experimental rats were sequentially advanced through the full behavioral protocol, which consisted of an exploration phase (2 d of free exploration on the maze with multiple randomly distributed water rewards) and a paired training and testing phase (obtaining water rewards from 3 learned locations on the maze). Four control rats completed 3-5 d of the free exploration phase only. The cheeseboard

maze apparatus and training schedule were as previously described *(33)*. Training and exploration sessions were performed during the same phase of the light cycle (1000-1500h), with sleep sessions occurring immediately afterward.

Data acquisition and processing: Neurophysiological signals, up to 320 channels, were amplified, digitized continuously at 20 kHz using a head-stage directly attached to the array (based on RHD2000 Intan Technologies), and stored for off-line analysis with 16-bit format. Data were analyzed using MATLAB (MathWorks) and visualized using NeuroScope (neurosuite.sourceforge.net).

Hippocampal and cortical ripples, as well as cortical gamma, were detected based on the Free Moving Animal (http://fmatoolbox.sourceforge.net) toolbox sequential detection algorithm as follows: i) band-pass filtering at 90–150 Hz (ripples) or 50–90 Hz (gamma) and signal rectification (Butterworth 3rd order); ii) detection of events where the filtered envelope was twice higher than standard deviation (s.d.) of filtered traces; iii) selection of envelopes with peaks signal 4 times higher than s.d.; iv) selection of events with greater than 20 ms duration; v) elimination of events that were common to the ripple channel and a selected noise channel (an EMG electrode). Spindle detection was initiated by filtering a cortical channel between 10–20 Hz, and then rectifying and normalizing the signal. Spindle events were identified when the envelope was at least two s.d. above the baseline (for a minimum of 400 ms and a maximum of 3 s) and the peak envelope was at least 3 s.d. above the baseline. Detections were visually inspected for accuracy for each recording session.

Comodulograms of cross frequency coupling were computed based on a Gabor wavelet, followed by a Gaussian window convolution with duration matched to the frequency. The correlation matrix was calculated based on the magnitude of the wavelet components. Comparisons with $p < 0.05$ after Bonferroni-Holm correction for multiple comparisons were considered statistically significant. Spectrograms were generated using wavelet transformation (Gabor) and coherence was calculated using multi-taper time-frequency analysis (Chronux: http://chronux.org/). Significance of cross-correlograms was calculated using a modified convolution method *(37)*. An amplitude-threshold method was used to detect spikes from band-passed filtered data (0.25 – 2.5 kHz) and spike waveforms were retrieved from wideband files. Spike clustering and sorting were performed using KlustaKwik (klustakwik.sourceforge.net/). The instantaneous LFP phase was extracted by Hilbert transform and validated with wavelet transformation to ensure uniform phase distribution. Units were deemed to have phase-locking to LFP oscillations when $\alpha < 0.05$ and $\kappa > 0.1$ on Rayleigh's test of non-uniformity. Average values are reported as mean ± standard error of mean (s.e.m.), except for ripple duration, which was reported as mean ± standard deviation of mean (std). Comparisons between groups were performed using non-parametric tests (Wilcoxon rank sum test for 2 groups, and Kruskal-Wallis test for 3 groups). $P < 0.05$ was considered significant.

Supplementary Figures:

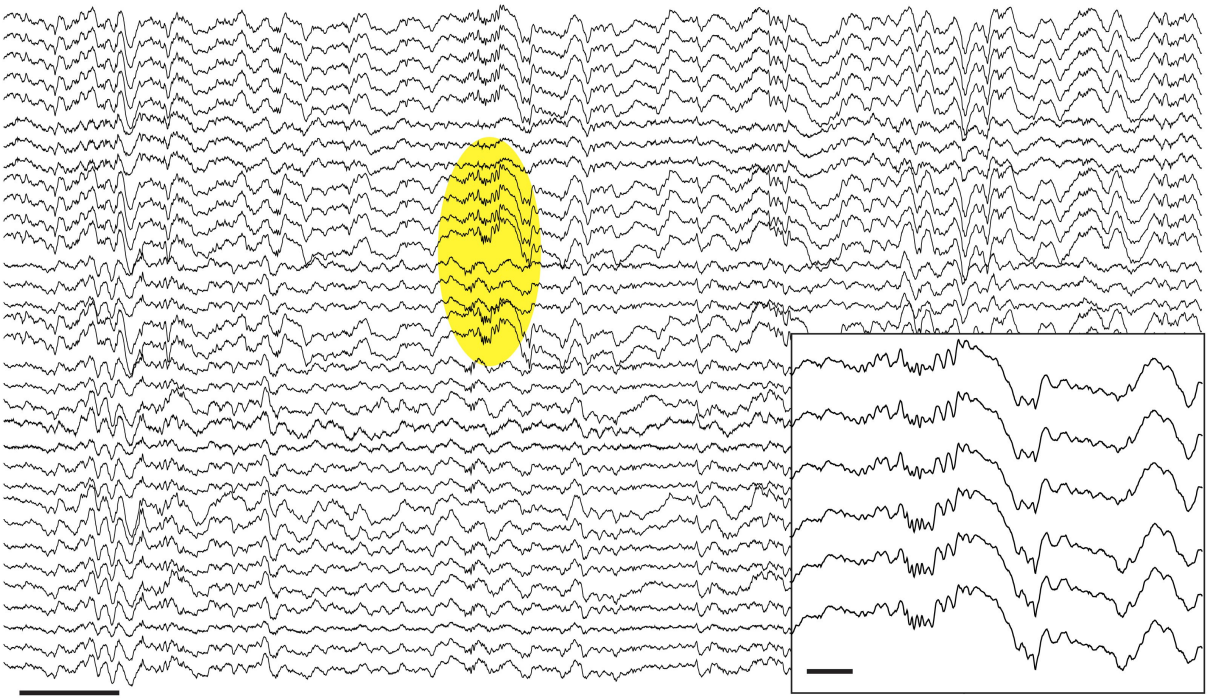

Supplementary Figure 1: Representative sample traces from a large-scale NeuroGrid.
LFP traces (0.1 – 1250 Hz) demonstrating occurrence of a cortical ripple localized to a subset of electrodes (yellow oval; scale bar: 500 ms). Inset shows the cortical ripple from the yellow oval magnified in time (scale bar: 50 ms).

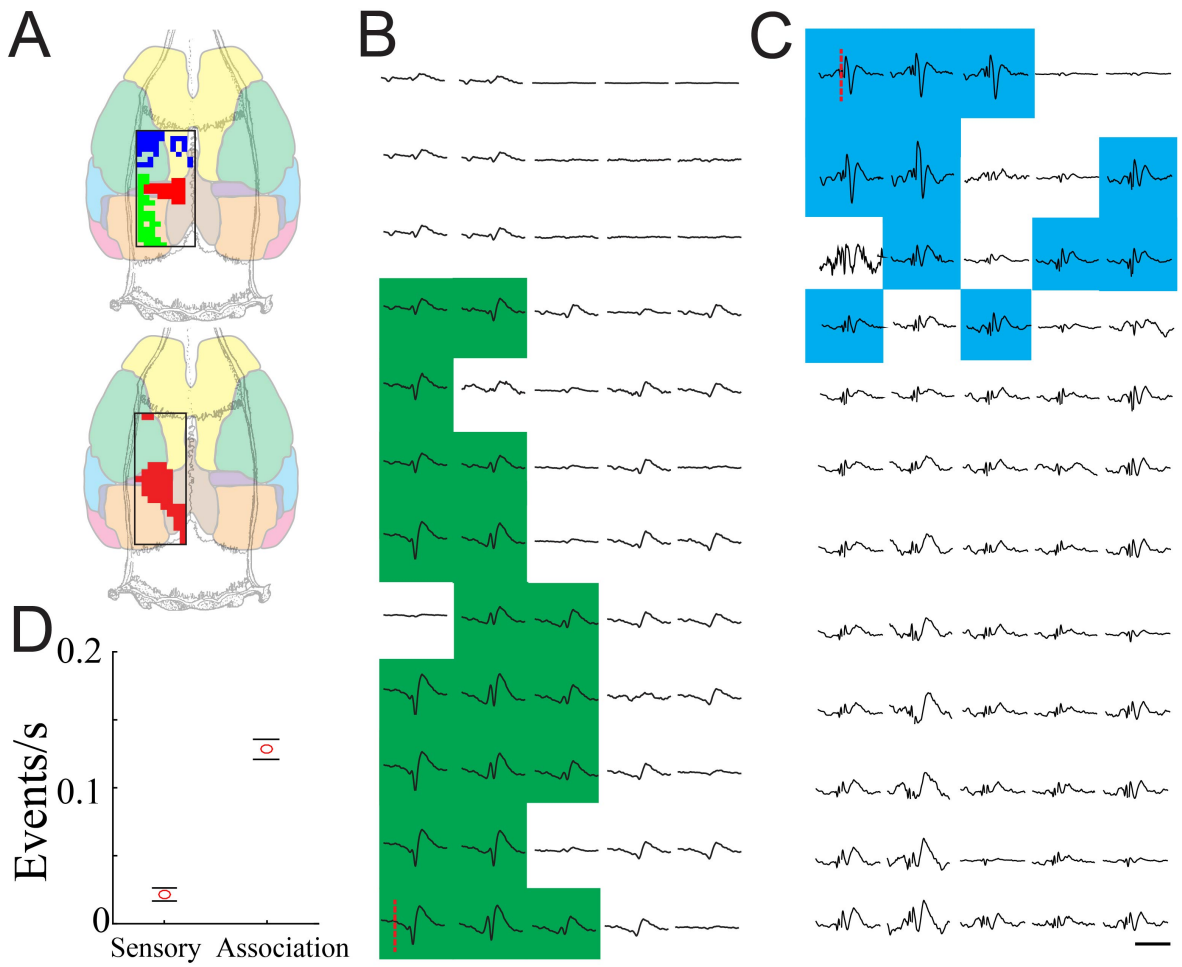

Supplementary Figure 2: Sensory evoked potentials and spatial localization of cortical ripples.

A) Anatomical map of neocortical ripple occurrence relative to maps of somatosensory and visual evoked responses. Two different rats than shown in **Figure 1C**. Electrodes with somatosensory and visual evoked potential amplitude with greater than 3 standard deviations above the mean amplitude (based on an average of 52 SSEP and 102 VEP trials) are colored blue and green, respectively. Regions with > 0.05 ripple events per second threshold are colored red.

B) Averaged visually evoked potentials (n = 102 trials) plotted spatially across the dorsal surface of the cortex with shaded electrodes showing above threshold evoked potentials (sample 5 × 12 out of 10 × 24 electrodes, left is lateral and right is medial; scale bar 100 ms; dashed line represents time of stimulus).

C) Averaged somatosensory evoked potentials (n = 52 trials) plotted spatially across the dorsal surface of the cortex with shaded electrodes showing above threshold evoked potentials (same rat as (B), but different sample 5 × 12 out of 10 × 24 electrodes, left is lateral and right is medial; scale bar 100 ms; stimulation artifacts are clipped; dashed line represents time of stimulus).

D) Average occurrence rate of cortical ripples in primary sensory vs. association cortices (0.13 ± 0.006 vs. 0.02 ± 0.004; Wilcoxon rank sum test, $p < 10^{-18}$; n = 3 sessions from 3 rats).

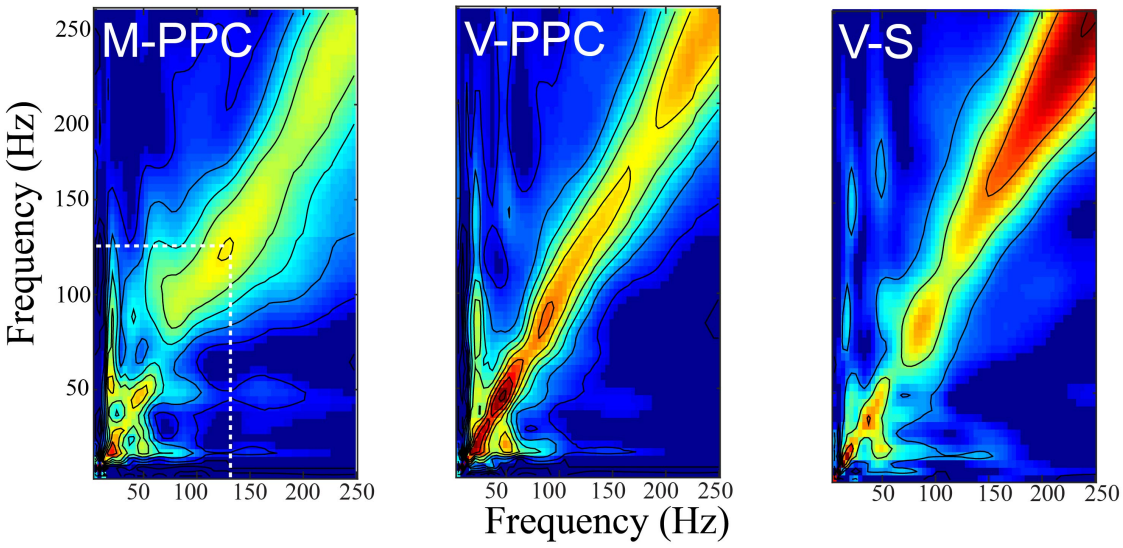

Supplementary Figure 3: Cortical comodulograms.
Sample comodulograms demonstrating cross frequency coupling between midline (M), parietal (PPC), primary visual (V), and somatosensory (S) cortices from the same time epoch. Note strong co-modulation centered at the ripple band between parietal and midline cortices; different rat from **Figure 1D**.

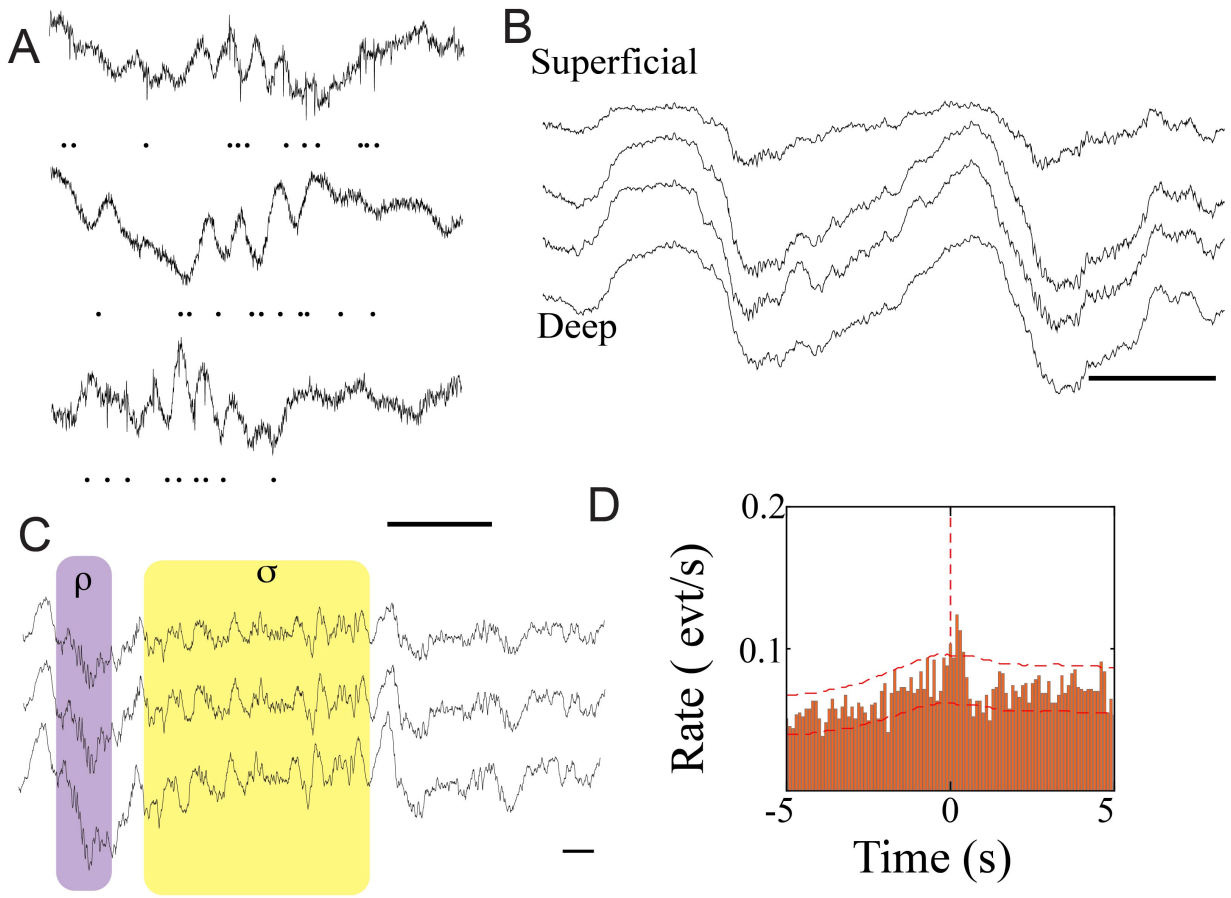

Supplementary Figure 4: Properties of cortical ripples.

A) Wide-band (0.1-7500 Hz) traces demonstrating sample cortical ripples and associated superimposed spiking activity recorded with a silicon probe (top) and high-density NeuroGrids (middle and bottom; examples from 3 different rats; dots show spike occurrence; scale bar 50 ms).

B) Depth profile of mPFC ripples recorded with a four-wire array across cortical layers. Distance between recording sites is 300 µm; scale bar 200 ms.

C) Wide-band LFP (0.1-1250 Hz) traces demonstrating sample mPFC cortical ripple coupled with spindle (scale bar 100 ms).

D) Cross-correlation between hippocampal ripples and sleep spindles (at time of peak power) during NREM sleep (red lines, 95% confidence intervals; n = 4197 hippocampal ripples, 2491 sleep spindles; single session in one rat).

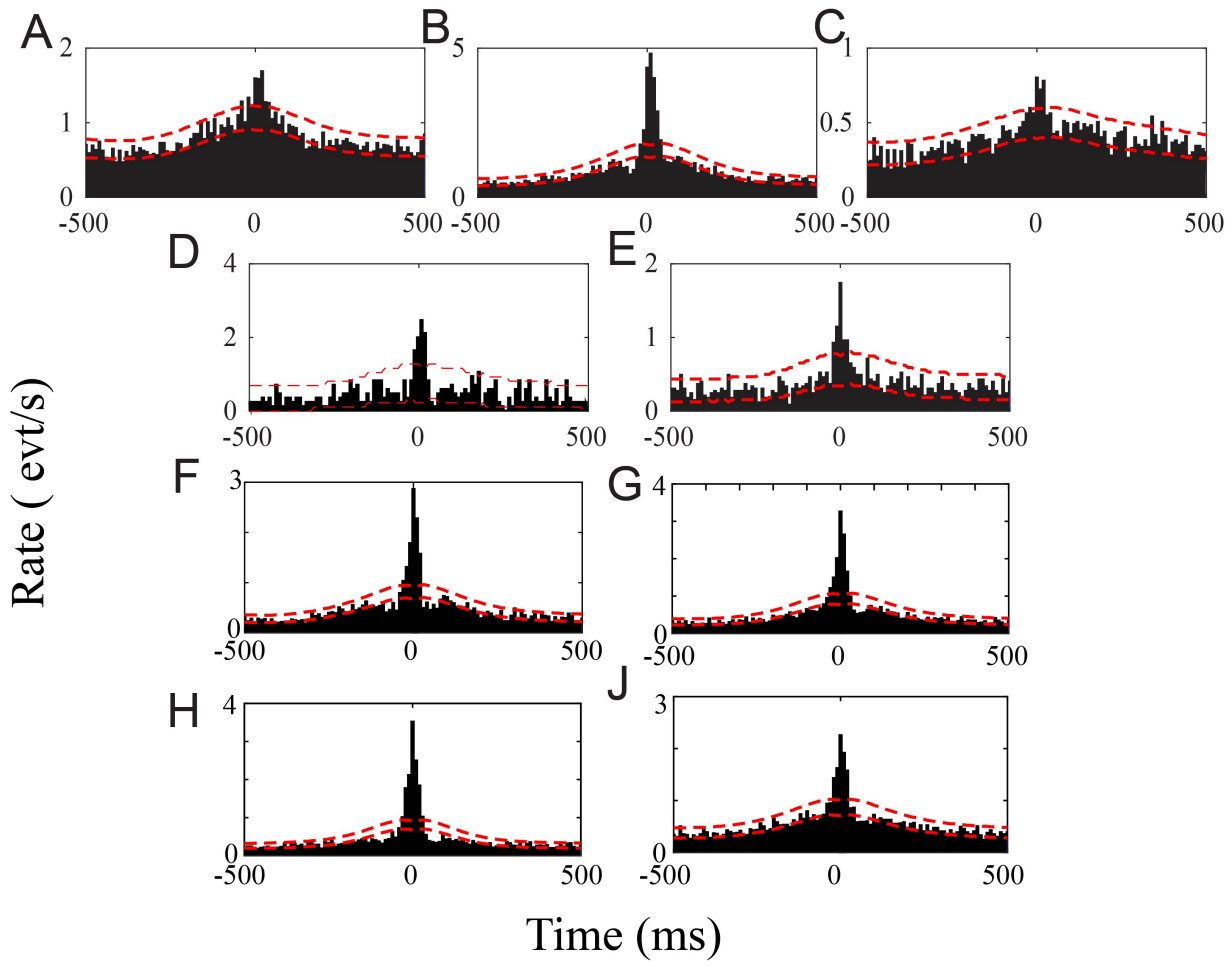

Supplementary Figure 5: Cross-correlation of hippocampal and cortical ripples in individual rats; different rats than in **Figure 2C;** red lines represent 95% confidence intervals.

RAT A = 12 sessions, 24952 cortical, 11551 hippocampal ripples;
RAT B = 4 sessions, 16658 cortical, 9193 hippocampal ripples;
RAT C = 4 sessions, 10719 cortical, 13779 hippocampal ripples;
RAT D = 4 sessions, 1083 cortical, 862 hippocampal ripples;
RAT E = 4 sessions, 5605 cortical, 2969 hippocampal ripples.
RAT F = 5 sessions, 12758 cortical, 13691 hippocampal ripples.
RAT G = 5 sessions, 14139 cortical, 15565 hippocampal ripples.
RAT H = 5 sessions, 13379 cortical, 1266 hippocampal ripples.
RAT J = 5 sessions, 11277 cortical, 10350 hippocampal ripples.

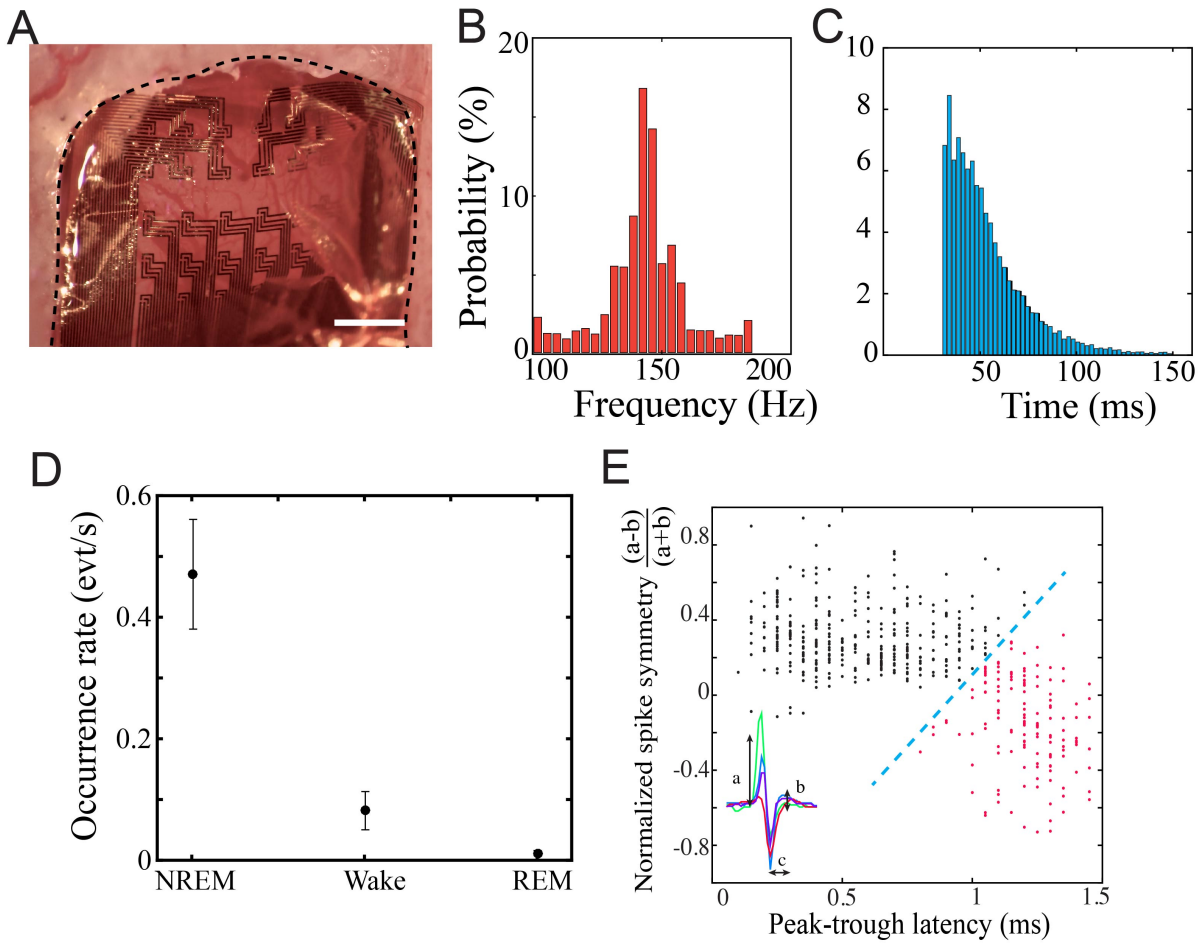

Supplementary Figure 6: Electrophysiological characterization of PPC ripples.

A) Micrograph of high-density NeuroGrid conforming to the surface of the rat brain. 5 × 6 'tetrode' electrodes, a subset of which are in focus (scale bar 500 μm).

B) Histogram of PPC ripple peak frequency (n = 252,343 ripples from 24 sessions in 6 rats).

C) Histogram of PPC ripple duration (n = 252,343 ripples from 24 sessions in 6 rats).

D) Occurrence rate of PPC ripples across behavior states (n = 12 sessions from 6 animals; mean ± standard error).

E) Scatterplot of waveform characteristics of putative neurons recorded from NeuroGrids and silicon probes. Waveform asymmetry and mean wide-band spike width were used to cluster neurons. Each dot corresponds to an average spike waveform of a putative isolated neuron. Waveform asymmetry is defined by the comparison of the peaks of the spike waveform (*a* and *b*), and spike duration is characterized by the latency of spike peak to spike trough (*c*). Dashed line indicates boundary between putative interneurons (black) and pyramidal cells (red). Neurons were not classified based on excitatory or inhibitory role in the cortex.

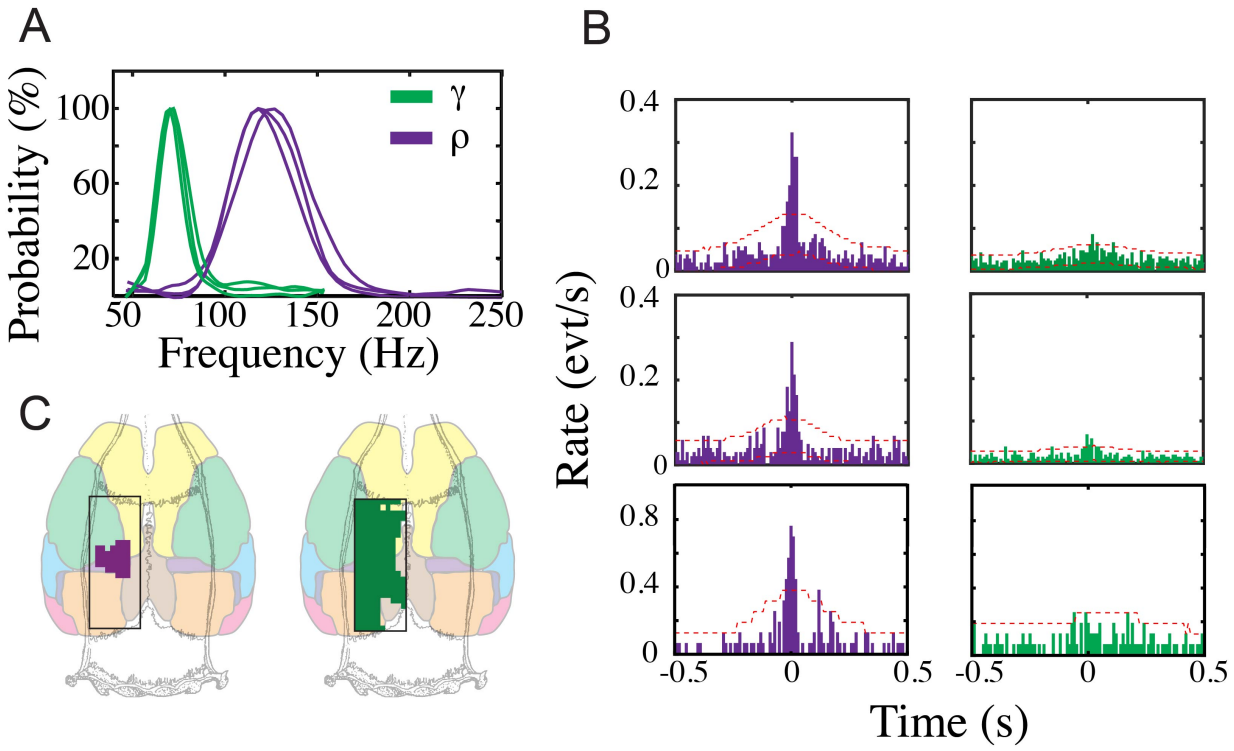

Supplementary Figure 7: Electrophysiological and spatial properties differentiate cortical gamma (50-90 Hz) and cortical ripple oscillations.

A) Histogram of PPC gamma peak frequencies (green; n = 747, 397, 1794 gamma oscillations from 3 sessions in 3 rats) compared to PPC ripple peak frequency (purple; n = 949, 243 and 1125 ripples from 3 sessions in 3 rats, respectively).

B) Cross-correlation of hippocampal and cortical ripples vs. hippocampal ripples and cortical gamma events. Top, n = 1794 gamma, 1056 HC ripples, 1125 cortical ripples. Middle, n = 747 gamma, 1041 HC ripples, 949 cortical ripples. Bottom, n= 397 gamma, 158 HC ripples, 243 cortical ripples. Red lines represent 95% confidence intervals.

C) Anatomical map of cortical ripple occurrence (left) relative to cortical gamma occurrence (right). Regions with > 0.05 ripple/gamma events per second are colored purple and green respectively. Different session from the same rat shown in Supplementary Fig. 2A.

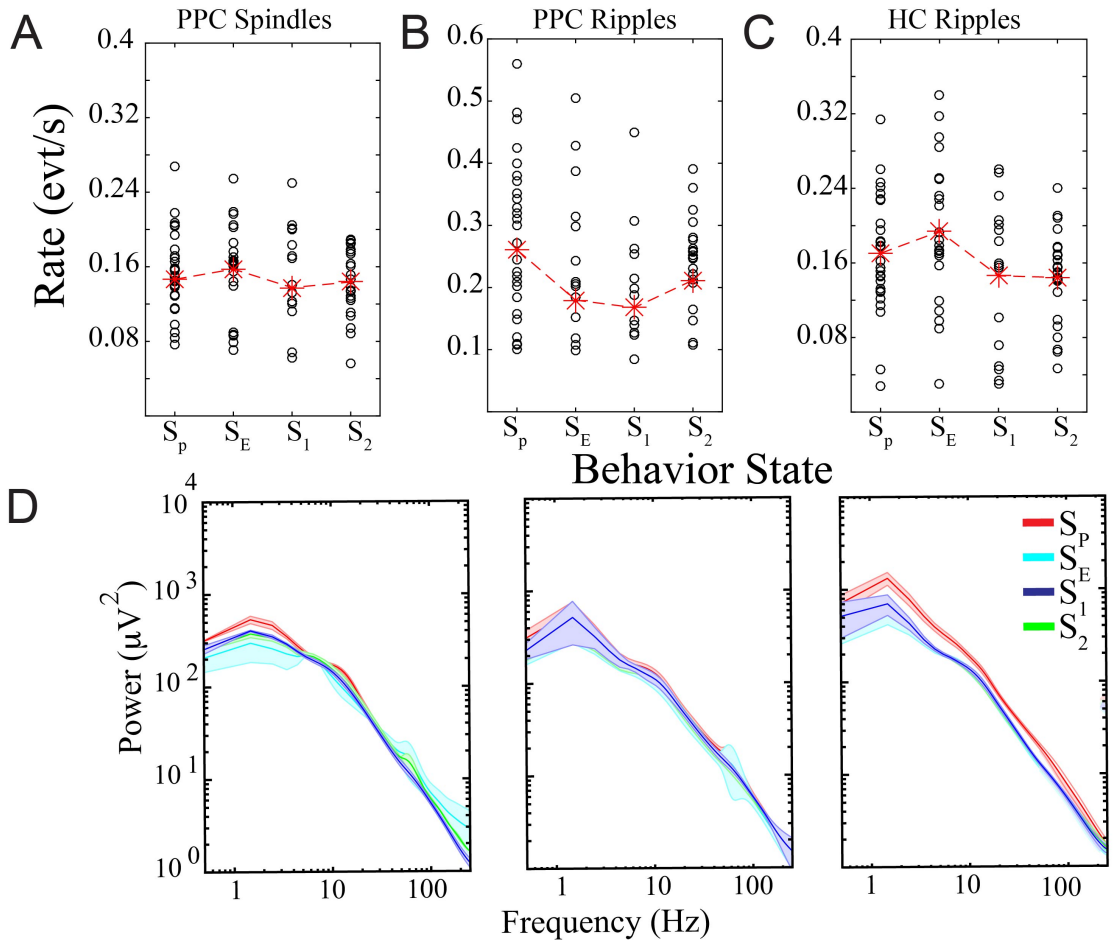

Supplementary Figure 8: Electrophysiological characterization of sleep across behavior states.

A) Occurrence rate of cortical spindles during NREM sleep after different behaviors (prior to protocol initiation (S_P), after exploration (S_E), after morning training session (S_1) and after afternoon training session (S_2); all sessions from 6 rats; open circles represent individual sessions and red stars show the mean).

B) Occurrence rate of cortical ripples during NREM sleep after different behaviors (all sessions from 6 rats).

C) Occurrence rate of hippocampal ripples during NREM sleep after different behaviors (all sessions from 6 rats).

D) Power spectra of NREM sleep after different behaviors (S_P = red; S_E = cyan; S_1 = blue; S_2 = green). Each panel represents an animal (n = 3; similar results for 3 additional rats), and each trace is the average power spectrum across sessions (n = 9-21 sessions per rat, 5 min per session; shading represents s.e.m.).

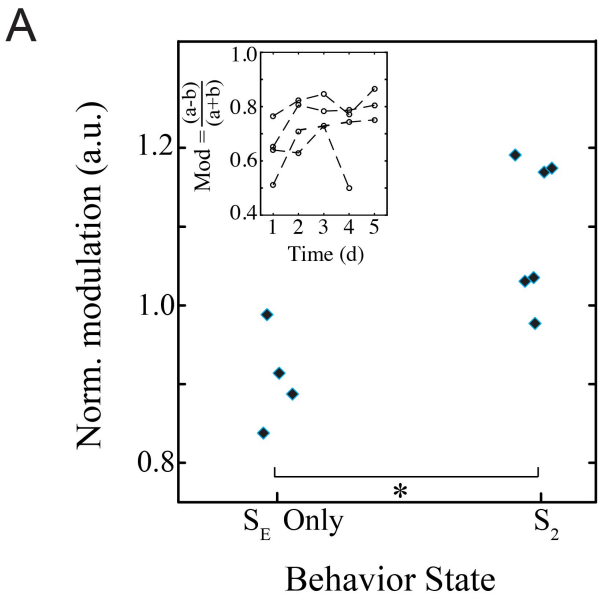

Supplementary Figure 9: Repeated sessions of exploration do not increase hippocampal-PPC ripple coupling.

Hippocampal-PPC ripple normalized coupling for control rats that underwent 3-5 consecutive days of exploration only (S_E only; n = 4) compared to rats that underwent 3-5 consecutive days of training and testing (Wilcoxon rank sum test, p = 0.019). Note that values from the S2 are from the same rats as represented in **Figure 4C**. Normalized coupling modulation was calculated by subtracting the average coupling strength of hippocampal and PPC ripples during sleep prior to initiation of behavior protocol from the coupling strength obtained during S_E for each rat (pooled over 3-5 days of exploration). Inset demonstrates changes in coupling for each individual rat.

References and Notes

1. R. D. Burwell, D. G. Amaral, Perirhinal and postrhinal cortices of the rat: Interconnectivity and connections with the entorhinal cortex. *J. Comp. Neurol.* **391**, 293–321 (1998). doi:10.1002/(SICI)1096-9861(19980216)391:3<293:AID-CNE2>3.0.CO;2-X Medline

2. R. L. Buckner, J. R. Andrews-Hanna, D. L. Schacter, The brain's default network: Anatomy, function, and relevance to disease. *Ann. N. Y. Acad. Sci.* **1124**, 1–38 (2008). doi:10.1196/annals.1440.011 Medline

3. I. Kahn, J. R. Andrews-Hanna, J. L. Vincent, A. Z. Snyder, R. L. Buckner, Distinct cortical anatomy linked to subregions of the medial temporal lobe revealed by intrinsic functional connectivity. *J. Neurophysiol.* **100**, 129–139 (2008). doi:10.1152/jn.00077.2008 Medline

4. G. Buzsáki, Hippocampal sharp wave-ripple: A cognitive biomarker for episodic memory and planning. *Hippocampus* **25**, 1073–1188 (2015). doi:10.1002/hipo.22488 Medline

5. T. Kitamura, S. K. Ogawa, D. S. Roy, T. Okuyama, M. D. Morrissey, L. M. Smith, R. L. Redondo, S. Tonegawa, Engrams and circuits crucial for systems consolidation of a memory. *Science* **356**, 73–78 (2017). doi:10.1126/science.aam6808 Medline

6. N. Maingret, G. Girardeau, R. Todorova, M. Goutierre, M. Zugaro, Hippnocampo-cortical coupling mediates memory consolidation during sleep. *Nat. Neurosci.* **19**, 959–964 (2016). doi:10.1038/nn.4304 Medline

7. T. Maviel, T. P. Durkin, F. Menzaghi, B. Bontempi, Sites of neocortical reorganization critical for remote spatial memory. *Science* **305**, 96–99 (2004). doi:10.1126/science.1098180 Medline

8. V. Ego-Stengel, M. A. Wilson, Disruption of ripple-associated hippocampal activity during rest impairs spatial learning in the rat. *Hippocampus* **20**, 1–10 (2010). Medline

9. G. Girardeau, K. Benchenane, S. I. Wiener, G. Buzsáki, M. B. Zugaro, Selective suppression of hippocampal ripples impairs spatial memory. *Nat. Neurosci.* **12**, 1222–1223 (2009). doi:10.1038/nn.2384 Medline

10. A. Peyrache, F. P. Battaglia, A. Destexhe, Inhibition recruitment in prefrontal cortex during sleep spindles and gating of hippocampal inputs. *Proc. Natl. Acad. Sci. U.S.A.* **108**, 17207–17212 (2011). doi:10.1073/pnas.1103612108 Medline

11. D. V. Wang, S. Ikemoto, Coordinated interaction between hippocampal sharp-wave ripples and anterior cingulate unit activity. *J. Neurosci.* **36**, 10663–10672 (2016). doi:10.1523/JNEUROSCI.1042-16.2016 Medline

12. A. G. Siapas, M. A. Wilson, Coordinated interactions between hippocampal ripples and cortical spindles during slow-wave sleep. *Neuron* **21**, 1123–1128 (1998). doi:10.1016/S0896-6273(00)80629-7 Medline

13. A. Sirota, J. Csicsvari, D. Buhl, G. Buzsáki, Communication between neocortex and hippocampus during sleep in rodents. *Proc. Natl. Acad. Sci. U.S.A.* **100**, 2065–2069 (2003). doi:10.1073/pnas.0437938100 Medline

14. N. K. Logothetis, O. Eschenko, Y. Murayama, M. Augath, T. Steudel, H. C. Evrard, M. Besserve, A. Oeltermann, Hippocampal-cortical interaction during periods of subcortical silence. *Nature* **491**, 547–553 (2012). doi:10.1038/nature11618 Medline

15. D. Khodagholy, J. N. Gelinas, Z. Zhao, M. Yeh, M. Long, J. D. Greenlee, W. Doyle, O. Devinsky, G. Buzsáki, Organic electronics for high-resolution electrocorticography of the human brain. *Sci. Adv.* **2**, e1601027 (2016). doi:10.1126/sciadv.1601027 Medline

16. D. Khodagholy, J. N. Gelinas, T. Thesen, W. Doyle, O. Devinsky, G. G. Malliaras, G. Buzsáki, NeuroGrid: Recording action potentials from the surface of the brain. *Nat. Neurosci.* **18**, 310–315 (2015). doi:10.1038/nn.3905 Medline

17. G. Buzsáki, D. L. Buhl, K. D. Harris, J. Csicsvari, B. Czéh, A. Morozov, *Neuroscience* **116**, 201–211 (2003). doi:10.1016/S0306-4522(02)00669-3 Medline

18. R. T. Canolty, E. Edwards, S. S. Dalal, M. Soltani, S. S. Nagarajan, H. E. Kirsch, M. S. Berger, N. M. Barbaro, R. T. Knight, High gamma power is phase-locked to theta oscillations in human neocortex. *Science* **313**, 1626–1628 (2006). doi:10.1126/science.1128115 Medline

19. S. Fujisawa, G. Buzsáki, A 4 Hz oscillation adaptively synchronizes prefrontal, VTA, and hippocampal activities. *Neuron* **72**, 153–165 (2011). doi:10.1016/j.neuron.2011.08.018 Medline

20. Y. Isomura, A. Sirota, S. Özen, S. Montgomery, K. Mizuseki, D. A. Henze, G. Buzsáki, Integration and segregation of activity in entorhinal-hippocampal subregions by neocortical slow oscillations. *Neuron* **52**, 871–882 (2006). doi:10.1016/j.neuron.2006.10.023 Medline

21. O. Eschenko, W. Ramadan, M. Mölle, J. Born, S. J. Sara, Sustained increase in hippocampal sharp-wave ripple activity during slow-wave sleep after learning. *Learn. Mem.* **15**, 222–228 (2008). doi:10.1101/lm.726008 Medline

22. L. Menendez de la Prida, R. J. Staba, J. A. Dian, Conundrums of high-frequency oscillations (80-800 Hz) in the epileptic brain. *J. Clin. Neurophysiol.* **32**, 207–219 (2015). doi:10.1097/WNP.0000000000000150 Medline

23. J. A. Blanco, M. Stead, A. Krieger, W. Stacey, D. Maus, E. Marsh, J. Viventi, K. H. Lee, R. Marsh, B. Litt, G. A. Worrell, Data mining neocortical high-frequency oscillations in epilepsy and controls. *Brain* **134**, 2948–2959 (2011). doi:10.1093/brain/awr212 Medline

24. C. Scheffzük, V. I. Kukushka, A. L. Vyssotski, A. Draguhn, A. B. L. Tort, J. Brankačk, Selective coupling between theta phase and neocortical fast gamma oscillations during REM-sleep in mice. *PLOS ONE* **6**, e28489 (2011). doi:10.1371/journal.pone.0028489 Medline

25. E. Stark, L. Roux, R. Eichler, Y. Senzai, S. Royer, G. Buzsáki, Pyramidal cell-interneuron interactions underlie hippocampal ripple oscillations. *Neuron* **83**, 467–480 (2014). doi:10.1016/j.neuron.2014.06.023 Medline

26. J. Csicsvari, H. Hirase, A. Czurkó, A. Mamiya, G. Buzsáki, Oscillatory coupling of hippocampal pyramidal cells and interneurons in the behaving Rat. *J. Neurosci.* **19**, 274–287 (1999). Medline

27. J. O'Keefe, L. Nadel, *The Hippocampus as a Cognitive Map* (PUBLISHER, 1978).

28. D. A. Nitz, Spaces within spaces: Rat parietal cortex neurons register position across three reference frames. *Nat. Neurosci.* **15**, 1365–1367 (2012). doi:10.1038/nn.3213 Medline

29. J. R. Whitlock, R. J. Sutherland, M. P. Witter, M. B. Moser, E. I. Moser, Navigating from hippocampus to parietal cortex. *Proc. Natl. Acad. Sci. U.S.A.* **105**, 14755–14762 (2008). doi:10.1073/pnas.0804216105 Medline

30. J. L. Calton, J. S. Taube, Where am I and how will I get there from here? A role for posterior parietal cortex in the integration of spatial information and route planning. *Neurobiol. Learn. Mem.* **91**, 186–196 (2009). doi:10.1016/j.nlm.2008.09.015 Medline

31. D. Dupret, J. O'Neill, B. Pleydell-Bouverie, J. Csicsvari, The reorganization and reactivation of hippocampal maps predict spatial memory performance. *Nat. Neurosci.* **13**, 995–1002 (2010). doi:10.1038/nn.2599 Medline

32. J. N. Gelinas, D. Khodagholy, T. Thesen, O. Devinsky, G. Buzsáki, Interictal epileptiform discharges induce hippocampal-cortical coupling in temporal lobe epilepsy. *Nat. Med.* **22**, 641–648 (2016). doi:10.1038/nm.4084 Medline

33. B. C. Carlyle, A. C. Nairn, M. Wang, Y. Yang, L. E. Jin, A. A. Simen, B. P. Ramos, K. A. Bordner, G. E. Craft, P. Davies, M. Pletikos, N. Šestan, A. F. T. Arnsten, C. D. Paspalas, cAMP-PKA phosphorylation of tau confers risk for degeneration in aging association cortex. *Proc. Natl. Acad. Sci. U.S.A.* **111**, 5036–5041 (2014). doi:10.1073/pnas.1322360111 Medline

34. A. Sirota, S. Montgomery, S. Fujisawa, Y. Isomura, M. Zugaro, G. Buzsáki, Entrainment of neocortical neurons and gamma oscillations by the hippocampal theta rhythm. *Neuron* **60**, 683–697 (2008). doi:10.1016/j.neuron.2008.09.014 Medline

35. F. P. Battaglia, G. R. Sutherland, B. L. McNaughton, Hippocampal sharp wave bursts coincide with neocortical "up-state" transitions. *Learn. Mem.* **11**, 697–704 (2004). doi:10.1101/lm.73504 Medline

36. A. A. Wilber, I. Skelin, W. Wu, B. L. McNaughton, Laminar organization of encoding and memory reactivation in the parietal cortex. *Neuron* **95**, 1406–1419.e5 (2017). doi:10.1016/j.neuron.2017.08.033 Medline

37. E. Stark, M. Abeles, Unbiased estimation of precise temporal correlations between spike trains. *J. Neurosci. Methods* **179**, 90–100 (2009). doi:10.1016/j.jneumeth.2008.12.029 Medline